Table S1. Summary of the field study transects (T). The coordinates are given based on Swiss coordinate system (or Swiss grid).

| Field campaign	Transect	Starting point (Easting, Northing)	Ending point (Easting, Northing)	Number of measurement points
22 September 2019	T2	(537524, 140687)	(537484, 149698)	10
22 September 2019	T2L	(535746, 140703)	(535678, 149702)	10
22 September 2019	T2R	(539874, 140691)	(539849, 149710)	10
23 September 2019	T2	(535746, 140703)	(537484, 149698)	10
23 September 2019	T2H	(528460, 146176)	(545498, 144617)	12
24 October 2019	T2	(535974, 140182)	(535926, 149197)	10
24 October 2019	T3	(522105, 136613)	(516003, 143554)	10
25 October 2019	T1	(550011, 139223)	(552114, 145753)	8
25 October 2019	T1H	(544996, 144517)	(554939, 141192)	8
25 November 2019	T1	(550690, 138496)	(550637, 146539)	9
25 November 2019	T2	(537197, 140678)	(535157, 149689)	10
25 November 2019	T3	(520675, 137339)	(520701, 144344)	8
3 September 2020	T6	(513241, 142532)	(516478, 139786)	Continuous
20 October 2020	T4	(525392, 138381)	(520668, 144837)	Continuous
20 October 2020	T5	(524640, 136585)	(522927, 140433)	Continuous
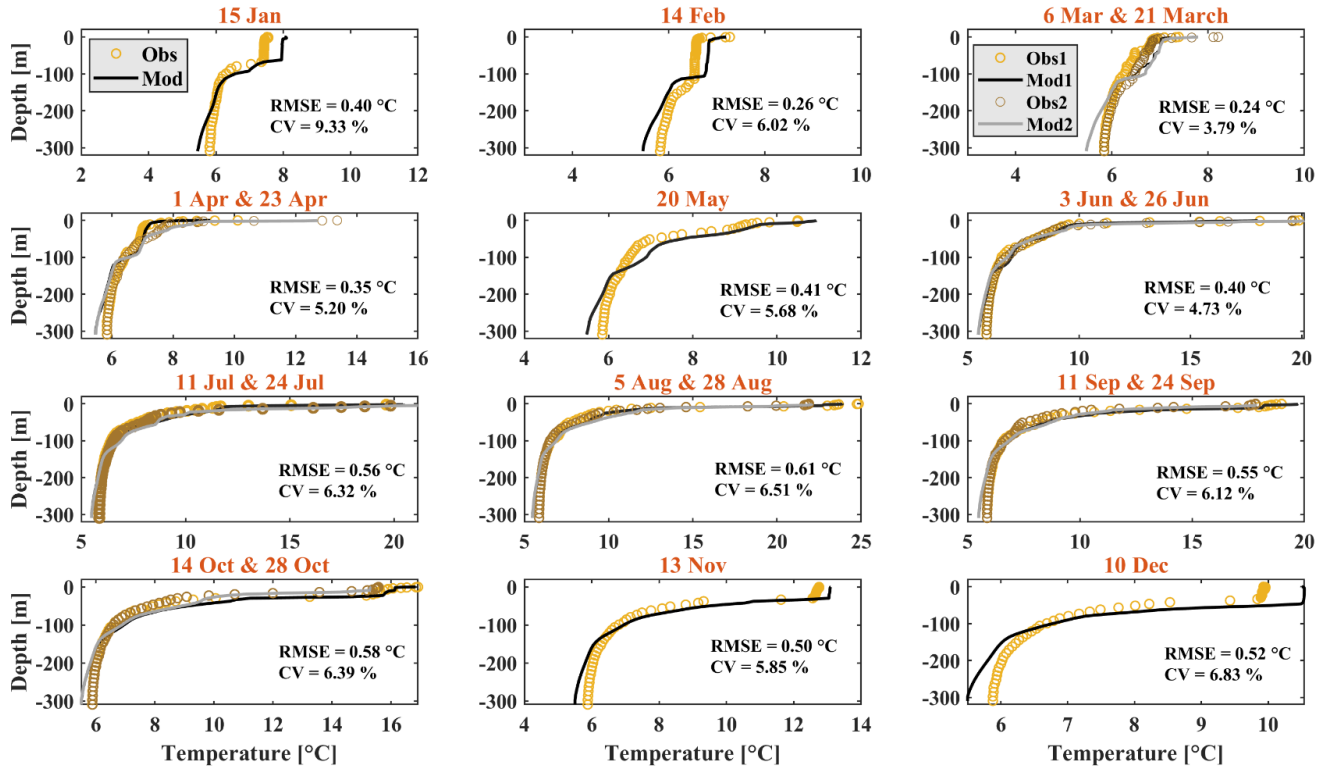
Figure S1. Comparison between observed (Obs1, 2: orange and brown circles) and modeled (Mod1, 2: black lines; see legends) temperature profiles at the CIPEL SHL2 monitoring station (for location, see Fig. 1b) in Lake Geneva for 2019. RMSE indicates the Root-Mean Square Error (RMSE) between observed and modeled temperature profiles. The Coefficient of Variation (CV) is the ratio of RMSE to the average of values observed, multiplied by 100.

S1: Synthetic Aperture Radar (SAR) imagery

The patterns observed in SAR images are due to the change of water surface roughness, which is influenced by wave/current interactions, natural surface films and spatial variations of the local wind field (Johannessen et al., 2005). Gyres or eddies that appear in SAR images as dark spiral features are called "black" or "classical" eddies (Karimova, 2012).

These dark features are associated with surfactant films or slicks that suppress short wind waves and thus reduce radar backscatter (Yamaguchi and Kawamura, 2009). At higher wind speeds (5-6 m/s at 10 m), wind-induced mixing in the upper layer will dissipate/redistribute the surface slicks, thus preventing the damping mechanism induced by the presence of surfactants (Dokken and Wahl, 1996; Johannessen et al., 1996). On the other hand, for C-band SAR imagery, little differentiation in surface roughness is evident for wind speeds below 3.25 ms^{-1} (Donelan and Pierson, 1987; Johannessen et al., 1996). In summary, SAR imagery can reveal gyres (more generally, surface current fields) under light wind conditions where the water surface is partially covered by (natural) surfactants. These conditions exist on Lake Geneva.

Caution should be taken when interpreting SAR images, since dark zones can also be due to non-uniformity in the surface wind field, e.g., (i) small-scale inhomogeneities of the near-surface wind field, (ii) wind shade, (iii) atmospheric convection, and (iv) atmospheric gravity waves (Moran et al., 2002; Wang et al., 2019). Therefore, we analyzed the available SAR imagery and selected images based on the prevailing wind field, and then combined these images with in situ observations and numerical modeling. In total, 78 images for 2016-2019 were obtained from the European Space Agency (ESA) Sentinel-1A and Sentinel-1B satellites for Lake Geneva.

As mentioned above, SAR imagery can aid in the detection of gyre boundaries. For example, the boundaries between two cyclonic (counterclockwise) gyres at the eastern part of lake, i.e., CG1 and CG2, can be determined using SAR data obtained from Sentinel-1 on 19 July and 12 October 2018 (Figure 4). Comparisons between the computed OW parameter from numerical results and the patterns observed in the SAR images are shown in Figure 4, where two (elliptical) gyres are evident. The minor/major axes of gyres CG1 and CG2 are approximately 6.5/12.9 and 9.8/15.9 km, respectively. Coriolis force plays an important role in the generation of these gyres, since their dimensions are much larger than the internal Rossby radius of deformation. The typical range of the internal Rossby radius for Lake Geneva is O(5 km) during the strongly stratified season and O(1 km) during the weakly stratified season (Lemmin and D'Adamo, 1996; Cushman-Roisin and Beckers, 2011).

S2: EOF analysis for the November and October 2019 campaigns

The first mode of the Empirical Orthogonal Function (EOF) analyses and the corresponding principal component time series for OW_N at 10-m depth and the first mode of the EOF analyses of wind stress for October and November 2019 are displayed in Figure S4. Patterns similar to those observed for September 2019 (Figure S3), with the three main gyres (AG, CG1, and CG2), are evident in the first mode of EOF results for November 2019. The principal component time series corresponding to the spatial pattern for October 2019 indicates that the amplitude of the vorticity-dominated regime suddenly increased a few hours after the *Bise* event (marked by vertical green lines) started to decrease, whereas the amplitude of the vorticity-dominated regime for the November event gradually increased after the first peak of wind stress. The vorticity-dominated signature in the center of the lake persisted for almost 7 d after the *Bise* event until a strong *Vent* wind coming from the opposite direction started (Figure S4). The *Bise* wind pattern was approximately the same as that observed in September 2018 (Figure 5). However, the zones where the maximum wind stress is concentrated are at different locations. During October and November 2019, the maximum wind stress was observed near the center of lake, whereas it was mainly concentrated on the western part of lake, i.e., the *Petit Lac* basin in September 2019 (Figure S3).
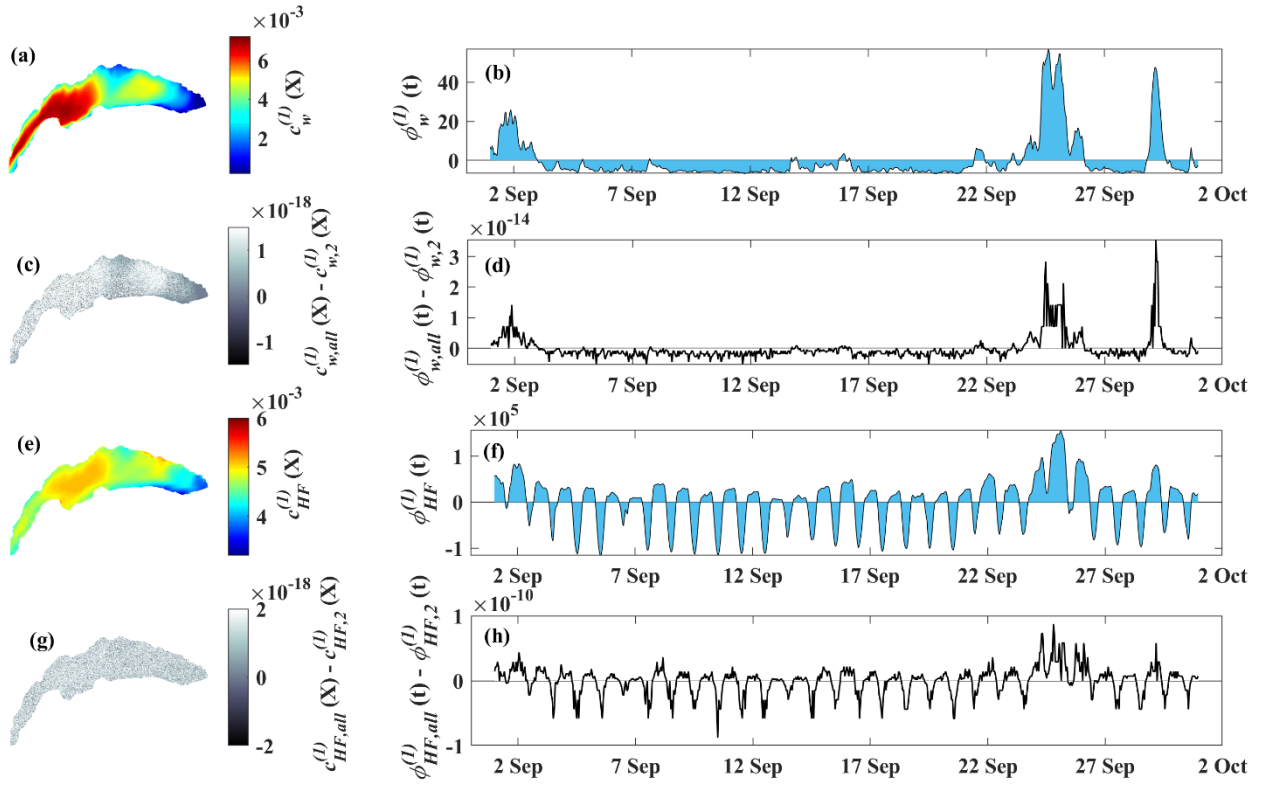
Figure S2. For September 2018 in Lake Geneva: (a) First spatial mode and (b) principal component time series of the total wind stress ($\sqrt{\tau_x^2 + \tau_y^2}$) calculated from COSMO atmospheric data. (c) first spatial modes and (d) principal component time series of noise between the solution with two dominant modes and the solution with all possible modes. (e) first spatial mode and (f) principal component time series of the net upward heat flux during the month of September 2018. (g) first spatial mode and (h) principal component time series of noise between the solution with two dominant modes and the solution with all possible modes for the net heat flux. The colorbars indicate the range of the parameters.
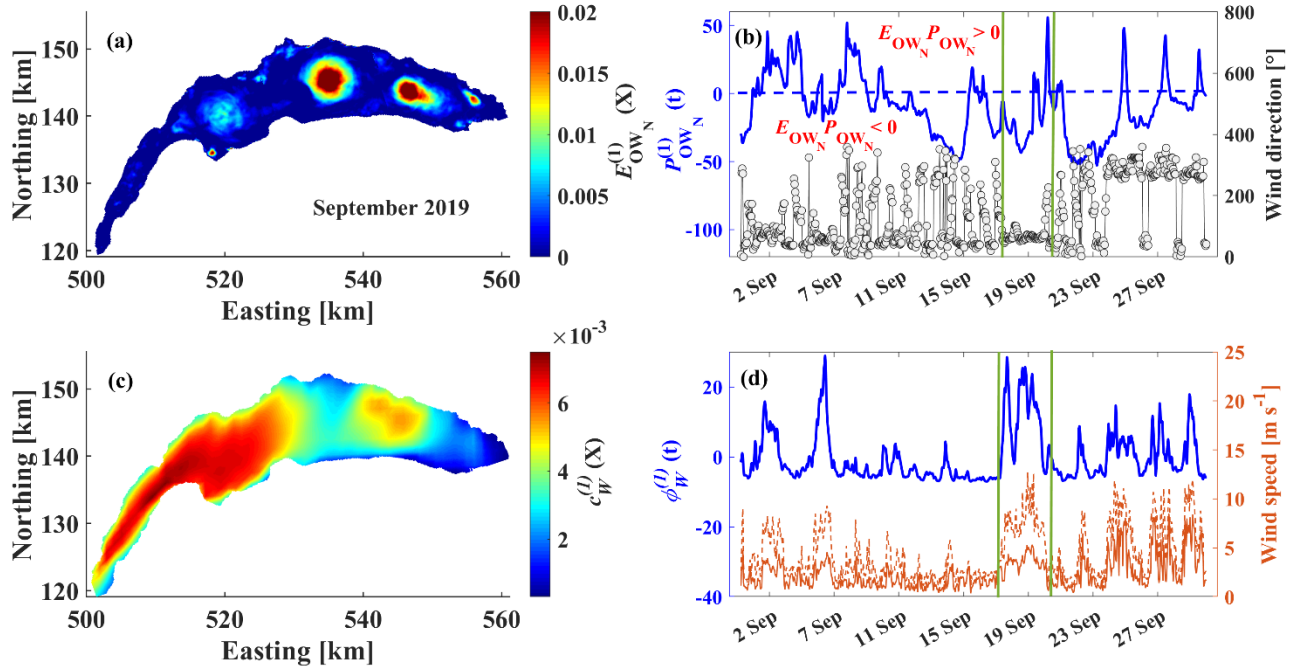
50

Figure S3. For September 2019: (a) First spatial mode of EOF and (b) principal component time series of the normalized Okubo-Weiss (OW$_N$) parameter at 10-m depth. (c) first spatial mode of EOF and (d) the principal component time series of total wind stress ($\sqrt{\tau_x^2 + \tau_y^2}$) calculated from the COSMO atmospheric data and the wind speed and direction measured at Buchillon station (for location, see Figure 1b). The first mode in (a) is dominated by the three large-scale gyres (circular zones of negative OW$_N$ values, i.e., $E_{OW_N}(X)P_{OW_N}(t) < 0$). The colorbars indicate the range of the parameters.
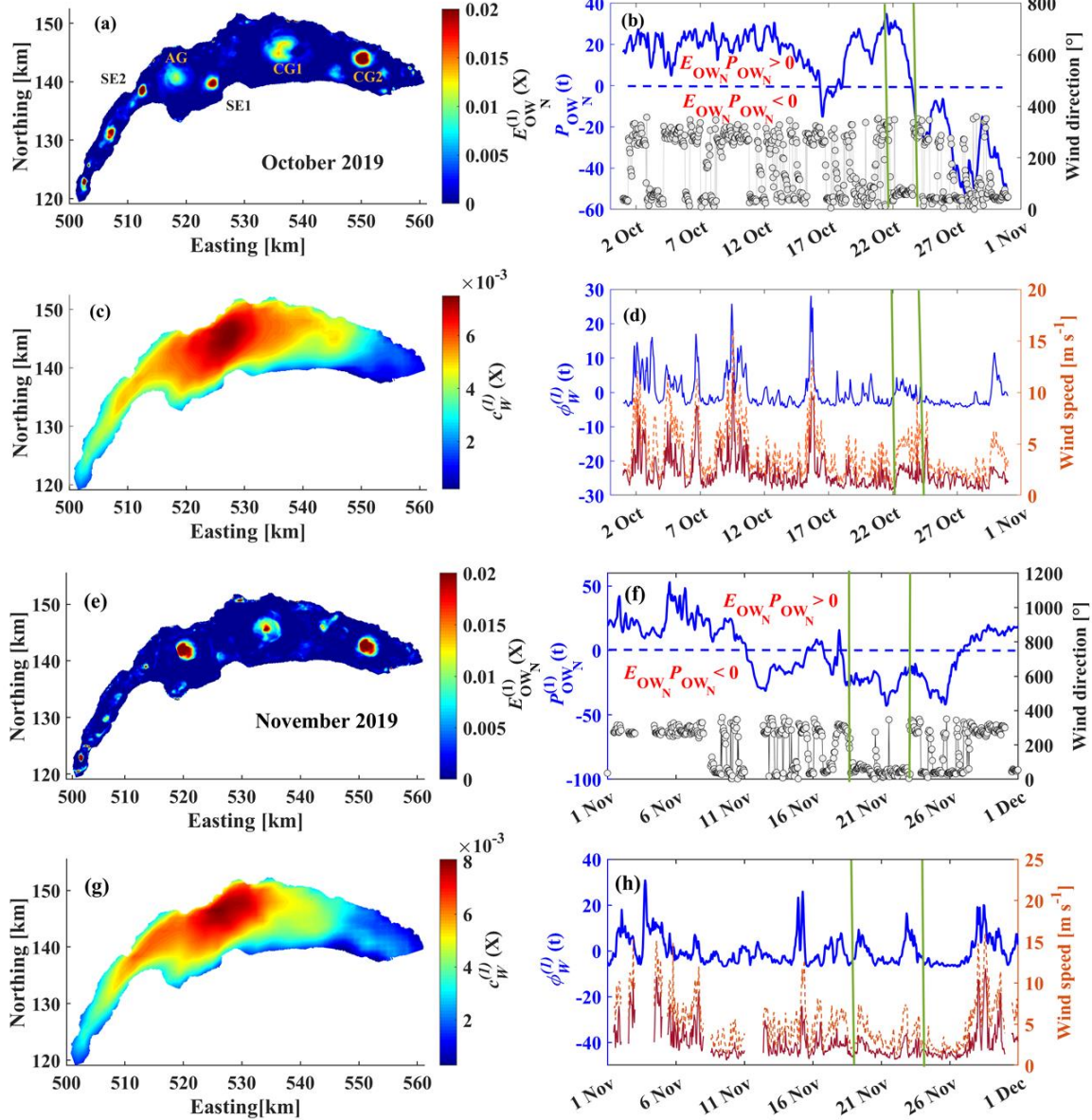
Figure S4. (a) First spatial mode of EOF and (b) corresponding principal component time series of OW_N at 10 m depth for October 2019. (c) First spatial mode of EOF and (d) corresponding principal component time series of the total wind stress ($\sqrt{\tau_x^2 + \tau_y^2}$) calculated from COSMO atmospheric data and the wind speed and direction measured at Buchillon station during October 2019. (e) First spatial mode of EOF and (f) principal component time series of OW_N at 10-m depth for November 2019. (g) First spatial mode of EOF and (h) corresponding principal component time series of the total wind stress and the wind speed and direction measured at Buchillon station during November 2019. Negative $E_{OW_N}P_{OW_N}$ indicates the presence of large-scale gyres and mesoscale eddies. The colorbars indicate the range of the parameters.
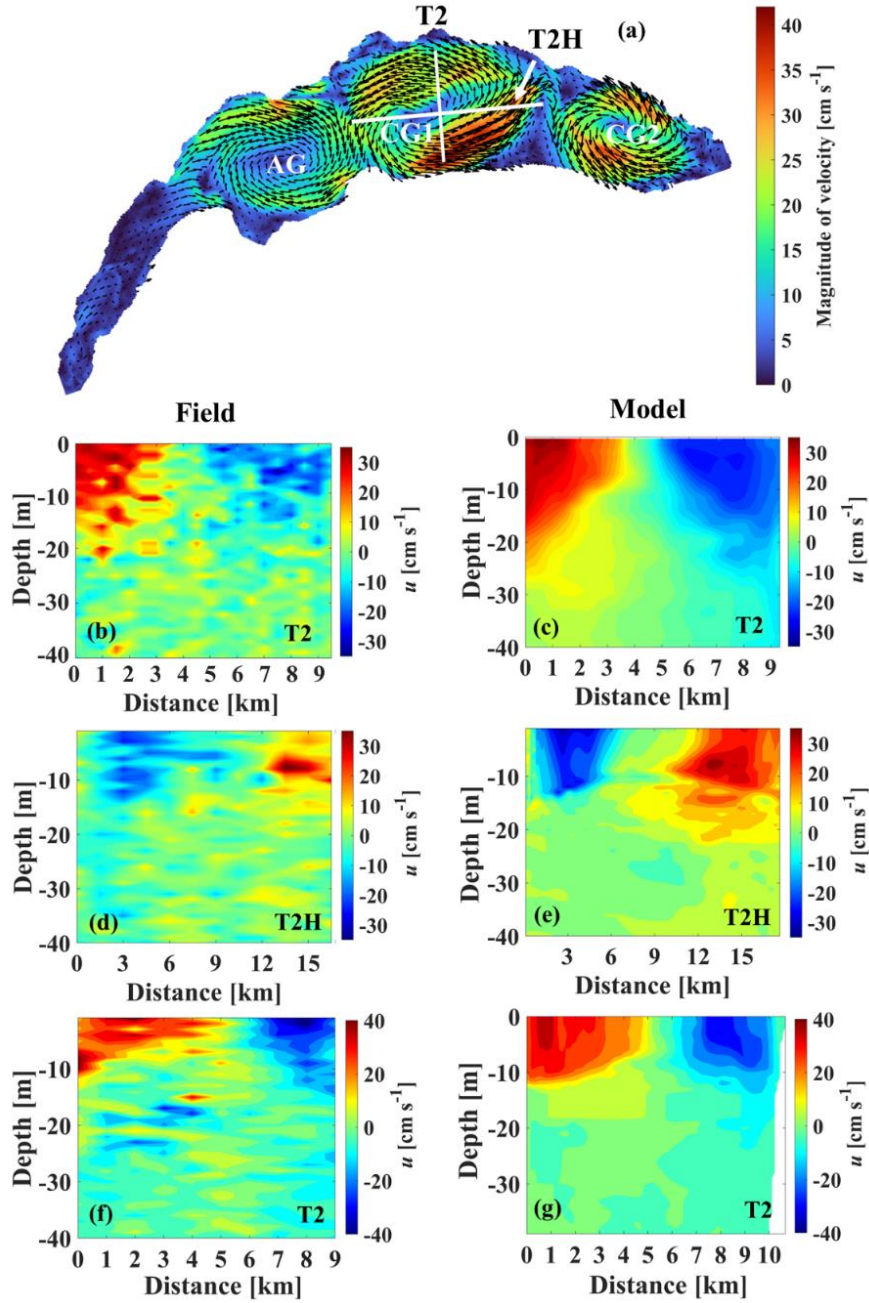
Figure S5. (a) Modeled surface velocity fields of the three-gyre (AG, CG1, CG2) pattern for 20 September 2019. (b) Measured horizontal velocity, and (c) corresponding modeled horizontal velocity along Transect T2 on 20 September. (d) Measured and (e) modeled horizontal velocity along T2H on 22 September. (f) Measured and (g) modeled horizontal velocity along T2 on 22 September. The colorbars indicate horizontal velocity in cm s^{-1}. Positive velocities are pointing eastward for transect, T2, and northward for transect T2H.
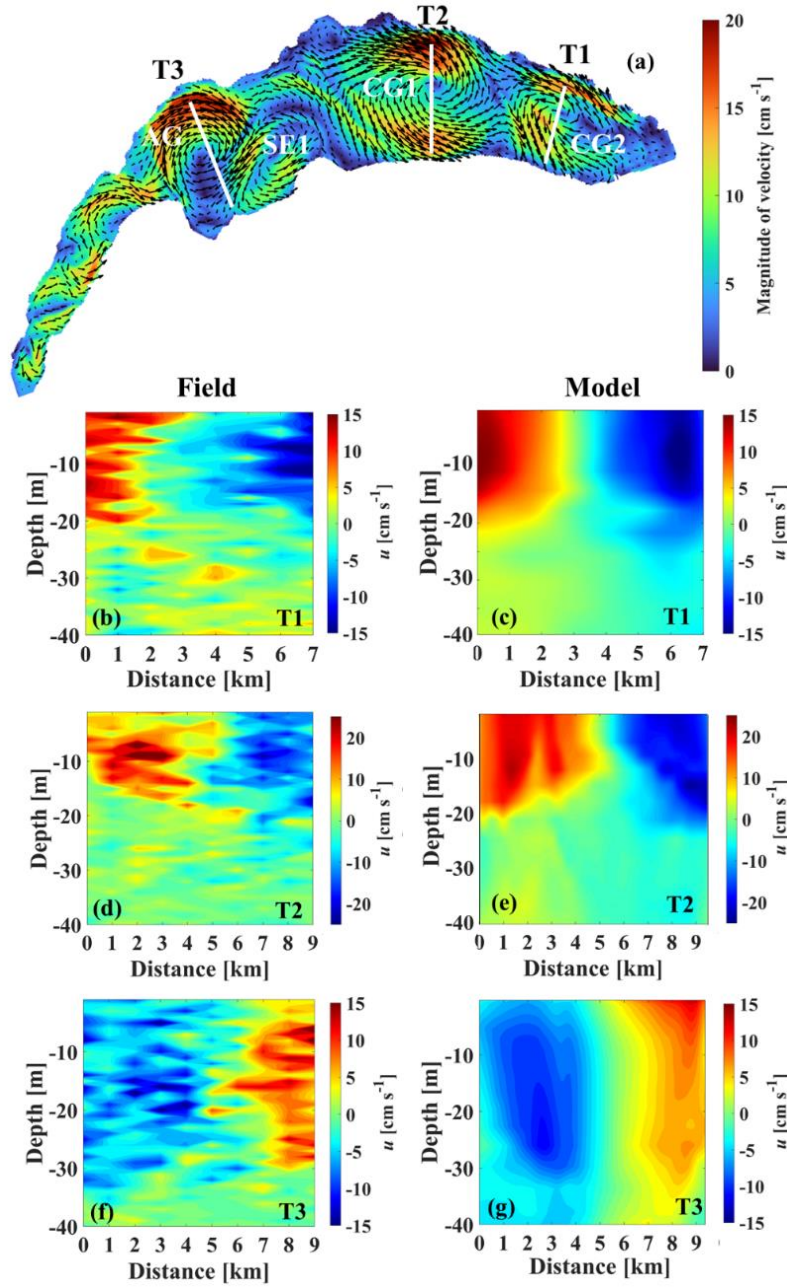
7

Figure S6. (a) Modeled surface velocity fields of the three gyre (AG, CG1, CG2) pattern for 24 October 2019. Black arrows show sense of rotation. (b) Measured horizontal velocity and, (c) corresponding modeled horizontal velocity along Transect T1 on 25 October 2019. (d) Measured and (e) modeled horizontal velocity along T2 on 24 October 2019. (f) Measured and (g) modeled horizontal velocity along T3 on 24 October 2019. The colorbars indicate horizontal velocity in cm s^{-1}. Positive velocities are pointing eastward. SE1 is a small eddy caught between gyres AG and CG1.
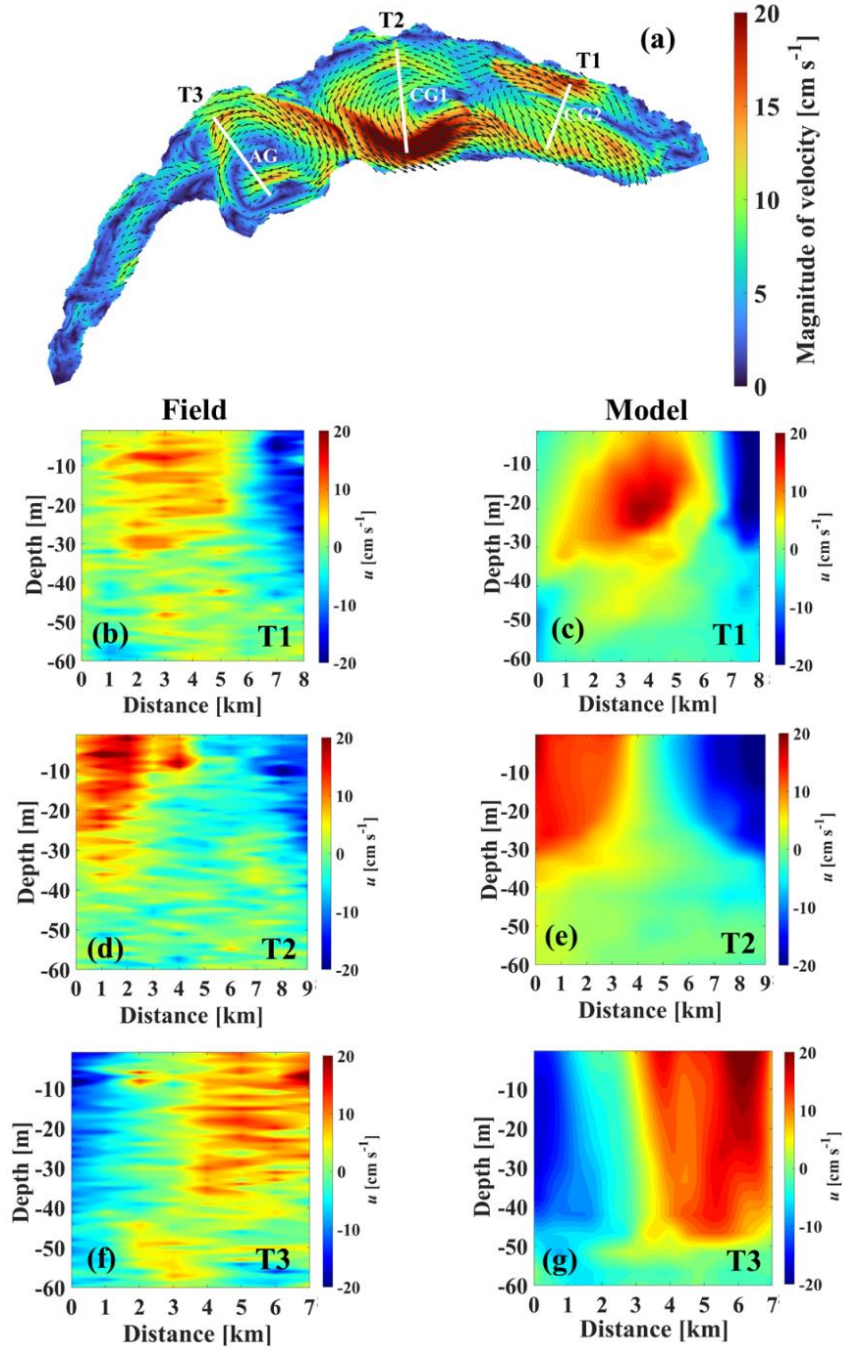
8

Figure S7. (a) Modeled surface velocity fields of three-gyre (AG, CG1, CG2) pattern for 25 November 2019. Black arrows show sense of rotation. (b) Measured horizontal velocity and (c) corresponding modeled horizontal velocity along Transect T1. (d) Measured and (e) modeled horizontal velocity along T2. (f) Measured and (g) modeled horizontal velocity along T3 for 25 November 2019. The colorbars indicate horizontal velocity in cm s^{-1}. Positive velocities are pointing eastward.